Proceedings of
11th European Conference on Turbomachinery Fluid dynamics & Thermodynamics
ETC11, March 23-27, 2015, Madrid, Spain

AEROACOUSTICAL AND FLOW ANALYSIS IN AN AUTOMOTIVE TURBOCHARGER CENTRIFUGAL COMPRESSOR BY CFD CALCULATIONS AND MEASUREMENTS

J.M. Desantes - A. Broatch - J. Galindo - R. Navarro

CMT - Motores Térmicos, Universitat Politècnica de València
Camino de Vera, 46022 Valencia, Spain, ronagar1@mot.upv.es

ABSTRACT

In the last decades, turbocharger technology has enabled the improvement of automotive internal combustion engines through downsizing, which promotes an interest in enlarging surge limit to increase engine low end torque. However, the operation in these conditions can be noisy. The objective of the work is the aeroacustical and flow analysis of a vaneless diffuser compressor by means of transient CFD calculations validated with experiments. Detached-eddy simulations from best efficiency to near surge conditions are performed. In the experimental apparatus, the compressor is installed in an anechoic chamber where dynamic pressure sensors located in the pipes allow the estimation of incoming and outgoing pressure waves. The results show that CFD calculations predict some features of experimental pressure spectra, whereas others are not properly captured. The model is also used to describe time-averaged flow field at different operating conditions. Also, a periodic oscillation of the detached boundary layer at blades suction side for best efficiency working point is found.

NOMENCLATURE

p pressure
u speed
a speed of sound
γ Ratio of specific heats
Subscripts
forw forward component
back backward component

INTRODUCTION

Most researchers consider that intake and exhaust systems are one of the main noise sources in passenger cars (Braun et al., 2013). Although downsizing and turbocharging has led to a reduction in internal combustion engines fuel consumption, it seems that this design approach increases powertrain radiated noise (Stoffels and Schroeer, 2003). The requirements of a high torque at low engine speeds has increased turbocharger compressor airborne noise (Evans and Ward, 2005), due to the shift of operating conditions towards surge line (Teng and Homco, 2009).

Compressor flow-induced acoustics is therefore becoming a major issue for automotive car makers. Researchers such as Evans and Ward (2005), Teng and Homco (2009) or Sevginer et al. (2007) identified turbocharger compressor NVH issues by measuring noise radiation. A common way to reduce noise radiation was the use of resonators in compressor outlet hose.

Computational Fluid Dynamics (CFD) is a tool that can be used to acquire a deeper understanding of centrifugal compressor aeroacoustics.

Mendonça et al. (2012) conducted a numerical study of turbocharger compressor flow-induced acoustics. A narrow band noise at a frequency about 70% of rotational speed was found, which is

produced by rotating stall phenomenon, i.e., a low momentum region that rotates at a slower speed than the impeller.

Bousquet et al. (2014) simulated three operating points of a centrifugal compressor, from peak efficiency to near stall conditions. A virtual probe linked to the relative relative frame located at 90% span at the impeller inlet was used for spectral analysis. Stator vane passing frequency tone is the main feature for the two operating conditions with higher mass flow. Near stall, a tone appears at a frequency 6 times the rotation order, which is due to the formation and shedding of 6 vortices per revolution.

Fontanesi et al. (2014) studied a turbocharger compressor with a compressor by-pass valve (CBV) using CFD. Two operating points at the same isospeed were investigated: one close to surge and the other at a two times higher mass flow rate. The case with higher mass flow provided a lower overall noise than the point close to surge at low frequency range (below 5 kHz). Both spectra include a narrow band noise at 2500 Hz, which is attributed to periodic flow detachment and re-attachment at the CBV junction. Experimental measurements also detected the aforementioned narrow band.

In this paper, detached eddy simulations (DES) of three centrifugal compressor operating points at same speed are performed in order to investigate their mean flow and acoustical features. The paper is organized as follows. First, the CFD model used in this paper is described. Comparison of time-averaged flow fields and acoustic signatures at different operating conditions is then performed. After that, the unsteady flow field phenomena at best efficiency point is investigated. Finally, paper conclusions are stated.

NUMERICAL MODEL

Figure 1 presents the numerical domain used in this paper, which includes an inlet pipe, impeller, hub cavity, vaneless diffuser, discharge volute and outlet duct. The impeller, diffuser and volute of the compressor were digitalized whereas the pipes were obtained by extruding the inlet and outlet cross sections, respectively, 5 diameters long. Backplate cavity along with tip clearance are also considered. Galindo et al. (2015) proved that CAD clearance can be safely used instead of actual tip clearance for centrifugal compressor noise predictions. The full domain, in which the impeller and the diffuser are 360° modeled, is meshed with 9.5 million polyhedral cells. Prism layer meshing has been used in order to increase near wall grid resolution so as to obtain y^+ values close to the unity in the impeller.

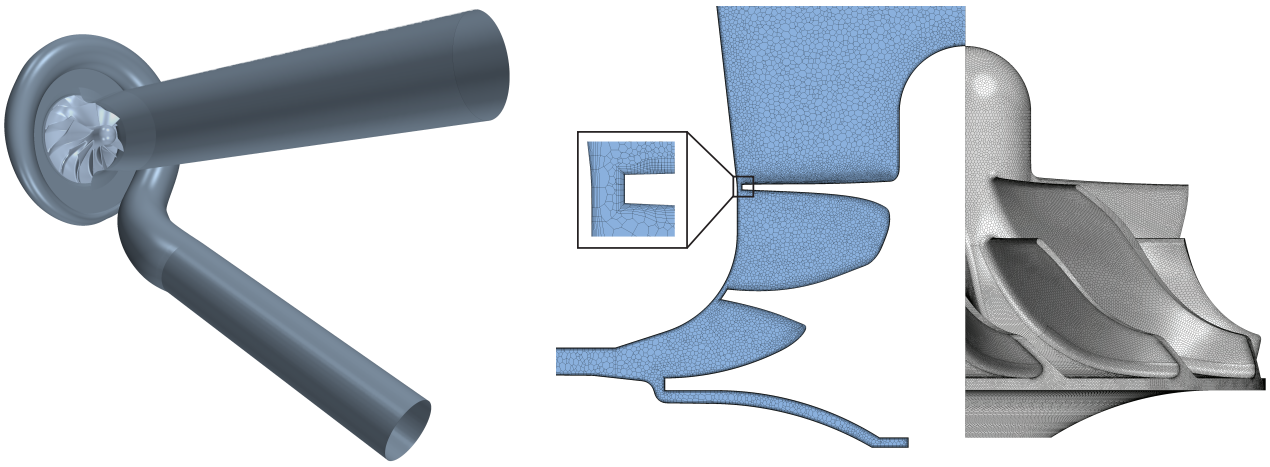

Figure 1: **Computational domain (left) and impeller mesh with a close-up of tip clearance boundary layer (right).**

Navarro (2014) conducted a mesh independence analysis at near-surge conditions, which revealed that increasing the cell count by a factor of two (until 19 million elements) provides global variables

(compression ratio, specific work and isentropic efficiency) with a relative difference below 1% when compared to the baseline 9.5 million cells mesh. In the same way, the finest mesh predicted a compressor acoustic signature with no significant differences from the one obtained using the 9.5 million elements grid.

The segregated solver of STAR-CCM+ (2014) was used to perform detached-eddy simulations with a SST $k-\omega$ turbulence model. Particularly, IDDES (Shur et al., 2008) is used, which combines WMLES and DDES hybrid RANS-LES approaches. Fixed outlet pressure, constant compressor speed of about 160 krpm (nominal speed) and inlet mass flow rate boundary conditions were used. 3 operating conditions at 1.4, 1.8 and 2.5 times surge mass flow at this speed were simulated, i.e., 60 g/s, 77 g/s and 109 g/s.

Rigid body motion approach was employed for the computations, in which heat transfer with the surroundings was neglected and smooth walls were considered. Second-order accurate transient solver was used with a time-step size so that the impeller mesh turns 1° per time step, since this time step is enough to resolve pressure spectra within human hearing range (up to 20 kHz)(Navarro, 2014). For more details of the computational set-up, please refer to the work of Navarro (2014).

With such a numerical model, compressor global variables can be predicted at different operating conditions with a relative error below 3% compared to experimental measurements (Navarro, 2014).

TIME-AVERAGED FLOW FIELD

The three simulated working points range from best efficiency point (BEP) to near-surge conditions for the compressor speed of 160 krpm. Time-averaged flow field provided by unsteady simulations is briefly described in this section in order to highlight the main differences between these operating conditions.

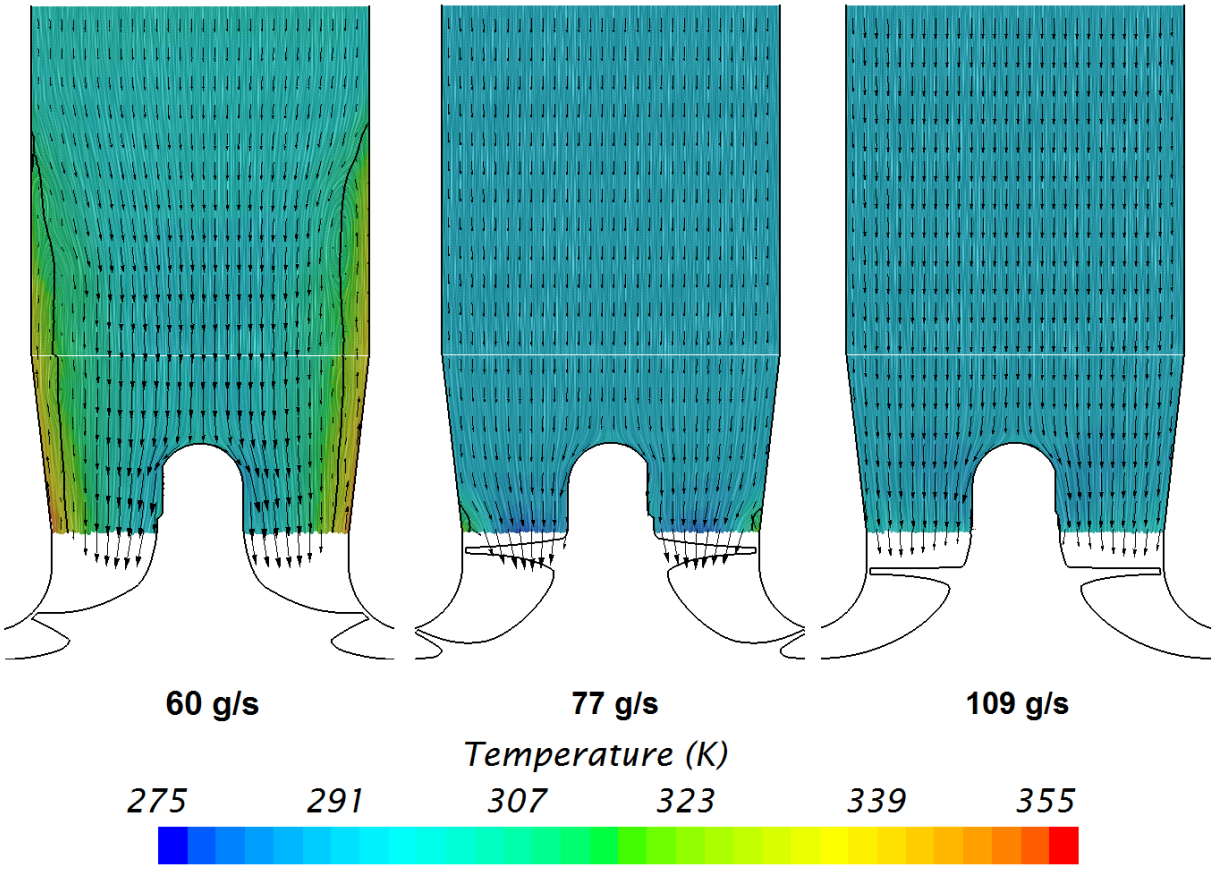

Figure 2: **LIC of velocity blended with temperature contours with velocity vectors at plane section for different operating conditions.**

Figure 2 shows the time-averaged inlet flow at a plane section for each operating point. The post-processing surface ends at the inducer plane. Line integral convolution (LIC) (Cabral and Leedom, 1993) blended with contours of temperature is plotted along with in-plane velocity vectors. A black solid line indicates a change of sign in axial velocity. Even the case with higher mass flow (109 g/s) presents backflows, but they are confined to the impeller periphery. At 77 g/s, recirculating flow surpasses the inducer plane, but it does not even reach the impeller's eye.

At 60 g/s, backflow region is thicker and extends 1 diameter upstream the impeller's eye (see Fig. 2). This recirculating flow is hotter than the incoming flow because it was partially compressed. Being a convective scalar quantity, temperature field is a good trace of backflow pattern and subsequent reintegration to the main flow. The use of the increase of temperature at the inlet duct wall as an indicator of the onset of compressor stall and surge has been investigated by several researchers. Andersen et al. (2008) showed that inlet temperature rise is detected by sensors close to the impeller even for operating conditions far from surge. Sensors located about two diameters upstream the inducer plane detect a temperature increase only in operating points close to surge, so they would be the best candidates to act as indicators of surge onset. Dehner et al. (2013) captured time-resolved temperature signals during mild and deep surge using fast-response thermocouples placed at the inlet duct axis. The sensor located at the inducer plane detects large temperature oscillations, occurring at the dominant frequency of the pressure pulsations.

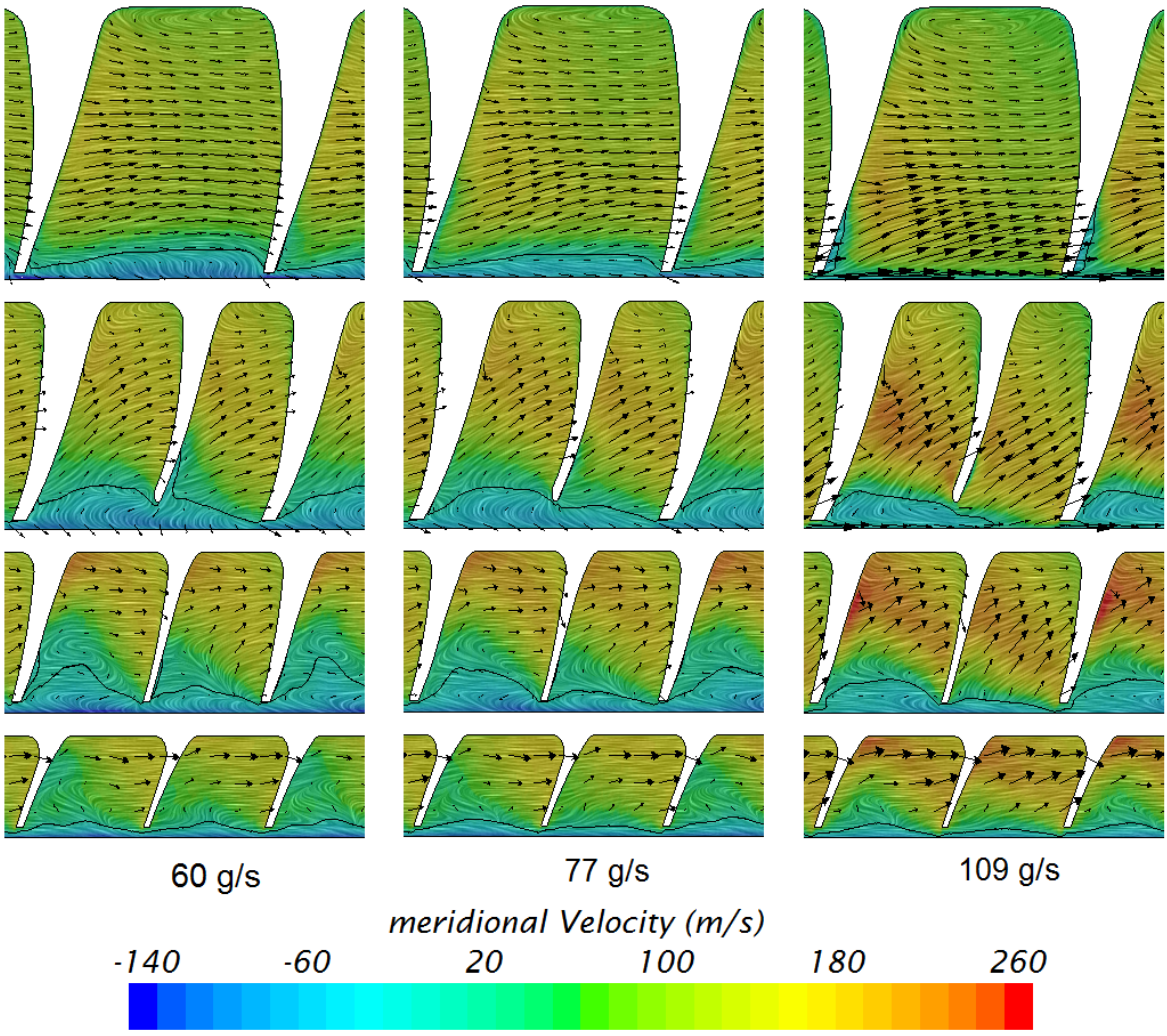

Figure 3: **LIC of relative velocity blended with meridional velocity contours with relative velocity vectors at a set of isomeridional surfaces for different operating conditions.**

Figure 3 presents flow at a set of 4 isomeridional cross-section for the different operating conditions. Relative velocity LIC is colored with meridional velocity and combined with relative velocity vectors. A solid black line indicates zero meridional velocity.

The onset of recirculating flow when the compressor works at 109 g/s is clearly located at the main blade leading edge suction side[1]. The positive incidence angle is responsible for the inception of the backflow, which spreads into the circumferential direction until reaching the splitter blade pressure side in the 3^{rd} cross-section. Flow pattern at 77 g/s and 60 g/s is alike except at the 1^{st} plane. At 77 g/s the incoming flow close to the recirculating region moves from shroud to hub because the turning point of the backflow is at a short axial distance (see Fig. 2), whereas the case with 60 g/s does not suffer from this phenomenon since the recirculating flow reintegrates much further upstream. Finally, flow migration from shroud to hub is more intense in the secondary passages, as can be noticed in the 3^{rd} and 4^{th} cross-sections of Fig. 3 for all operating conditions.

COMPRESSOR AEROACOUSTICS

The description of the time-averaged numerical solution performed in the previous section allows one to obtain an idea of the main compressor flow features. However, the temporal evolution of the unsteady calculations should be investigated if the understanding of phenomena resulting in the different noise mechanisms is sought.

Experimental apparatus

Experimental acoustic spectra are used as a reference for assessing the accuracy of the numerical model. A turbocharger test rig installed in an anechoic chamber was employed to obtain the experimental measurements shown in this paper. A detailed description of the gas stand is given by Galindo et al. (2006).

Figure 4 depicts a sketch of the turbocharger test rig, in which straight pipes placed at the inlet and outlet of the compressor are observed, along with piezoelectric pressure sensor arrays. A Yokogawa digital oscilloscope was used to sample these pressure signals at 100 kHz during 1 second at each operating condition.

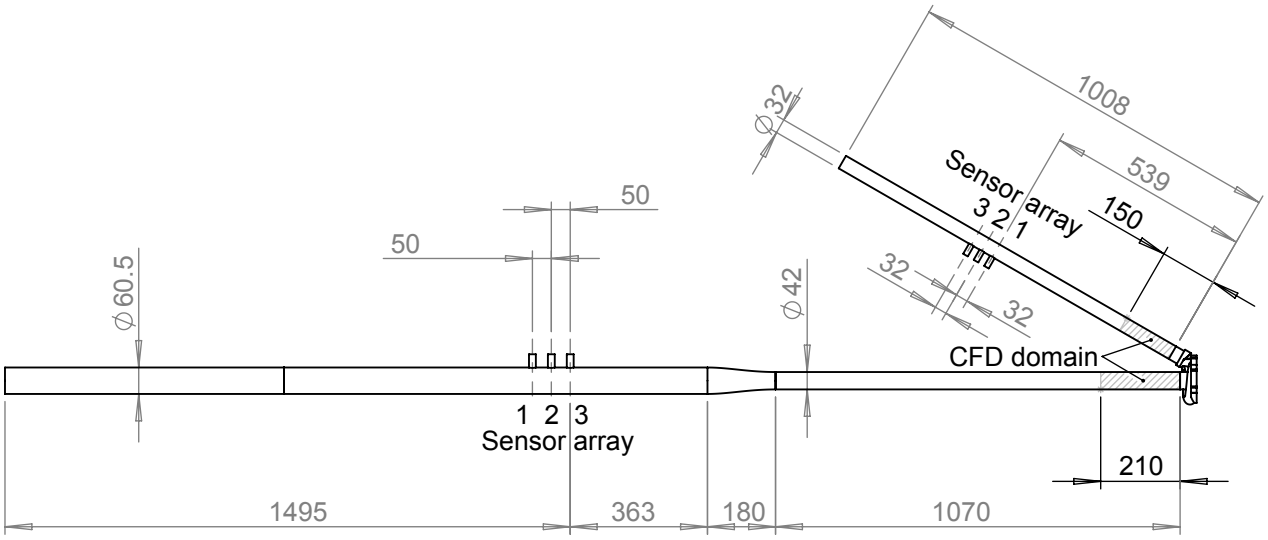

Figure 4: **Compressor piping layout, highlighting the CFD domain and the sensor arrays. Dimensions are in mm**

[1]In the unwrapped pictures of this paper, the projection of the compressor rotation becomes a translation from right to left. Therefore, in these pictures, blade pressure side is the left side of the blade whereas the right side of the blade is the suction side.

Inlet and outlet linear arrays of three piezoelectric sensors each were designed in accordance with Piñero et al. (2000). In this way, the pressure trace can be decomposed into a forward-traveling wave $p_{forw}(t)$ and a backward-traveling wave $p_{back}(t)$ by means of the beamforming-based signal analysis method developed by Piñero et al. (2000).

A full description of the experimental apparatus used to obtain the acoustical measurements was presented by Broatch et al. (2014).

Comparison of outlet pressure spectra

The methodology developed by Broatch et al. (2014) is used in order to obtain the compressor acoustic signature for the considered operating conditions. Pressure spectral densities (PSD) are estimated by means of Welch's overlapped segmented average (Welch, 1967). Hamming windowing is used at blocks with 50% overlap. For each operating condition, pressure signals are recorded after the achievement of a steady-state during no less than 150 impeller revolutions (more than 55 ms) and are then split into the number of blocks which provides the frequency resolution closest to 150 Hz. In this way, the calculated spectra are meaningful above 300 Hz.

The acoustic analysis is performed dividing the acoustic spectrum in two regions: plane wave range and high frequency range.

Plane wave range starts at the lowest frequency attainable and finishes with the onset of first asymmetric mode. The effect of standing waves on low frequency range spectra in numerical simulations is mitigated by the use of pressure decomposition (Broatch et al., 2014). As mentioned before, experimental signals are decomposed using the beamforming-based technique described by Piñero et al. (2000), although it imposes a constraint on maximum frequency (Broatch et al., 2014). Pressure components in CFD are obtained by means of the following expressions:

$$p_{forw} = p_{ref}\left[\frac{1}{2}\left(1+\left(\frac{p}{p_{ref}}\right)^{\frac{\gamma-1}{2\gamma}}\left(1+\frac{\gamma-1}{2}\frac{u}{a}\right)\right)\right]^{\frac{2\gamma}{\gamma-1}} \qquad (1)$$

$$p_{back} = p_{ref}\left[\frac{1}{2}\left(1+\left(\frac{p}{p_{ref}}\right)^{\frac{\gamma-1}{2\gamma}}\left(1-\frac{\gamma-1}{2}\frac{u}{a}\right)\right)\right]^{\frac{2\gamma}{\gamma-1}},$$

which are inspired by the Method of Characteristics (MoC), as described by Torregrosa et al. (2012). Averaging of flow field variables at inlet and outlet cross-sections is performed so as to obtain the pressure components.

High frequency range begins when the first asymmetric mode is cut on and is extended until 20 kHz. Broatch et al. (2014) showed that point monitors located at wall ducts should be used in this frequency range so as to capture higher order modes. Pressure decomposition (Eq. 1) is again used to obtain the numerical spectra in order to reduce the impact of standing waves, whereas experimental pressure traces cannot be decomposed and thus a single probe of each array is used to obtain the raw PSD.

Figure 5 presents the experimental and numerical outlet spectra for BEP. At the low frequency range, the measured spectrum presents a broadband elevation between 1 and 3 kHz. This feature is captured by both experiments and simulations at working points closer to surge (see Figs. 6 and 7); phenomenon known as *whoosh noise* (Evans and Ward, 2005; Teng and Homco, 2009). However, the numerical spectrum for BEP is *flat*, and overpredicts the experimental PSD.

In the high frequency range, experimental and numerical spectra are alike for all operating conditions (see Figs. 5 to 7): a tone exists at 16 kHz, corresponding to the main blade passing frequency, and the rest of the PSD amplitude is properly predicted. The only feature that the simulations miss is the broadband elevation between 13 and 16 kHz of the measured spectrum.

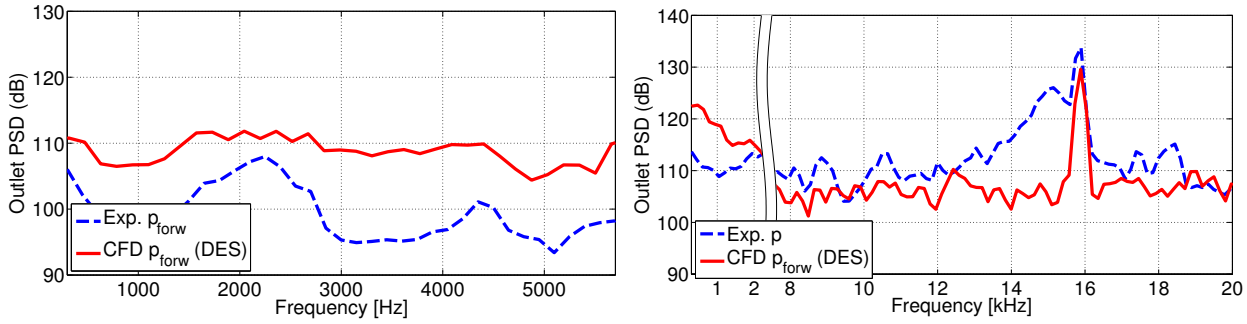

Figure 5: **PSD of experimental and numerical pressure at outlet duct, at low frequency (left) and high frequency (right) range, for 109 g/s operating point.**

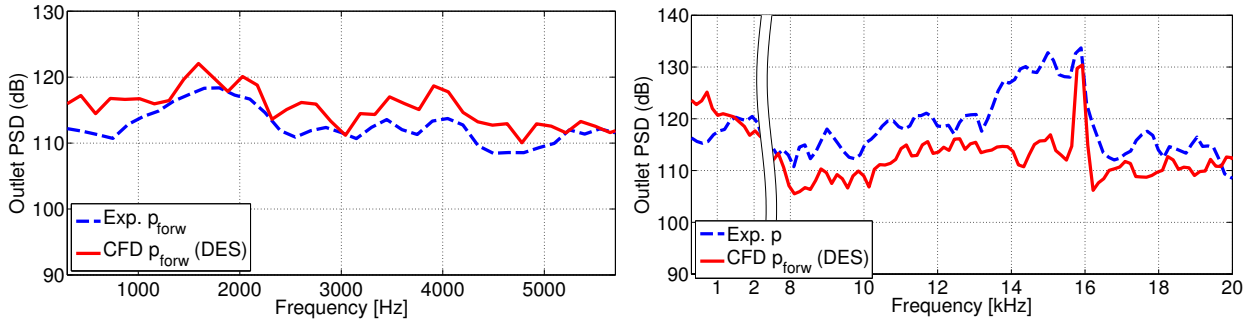

Figure 6: **PSD of experimental and numerical pressure at outlet duct, at low frequency (left) and high frequency (right) range, for 77 g/s operating point.**

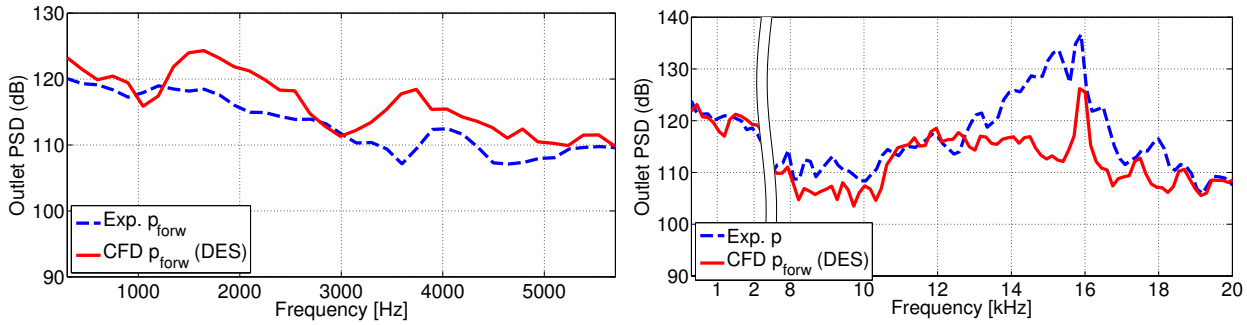

Figure 7: **PSD of experimental and numerical pressure at outlet duct, at low frequency (left) and high frequency (right) range, for 60 g/s operating point.**

Best efficiency point aeroacoustics

In this paper, the aeroacoustical analysis is limited to the point with highest mass flow rate (109 g/s). Flow-induced acoustics at operating conditions with less mass flow have been already investigated by Broatch et al. (2015). The numerical spectra showed in Fig. 5 presents no significant features. In any case, the 109 g/s simulation was investigated so as to search for unsteady phenomena.

The fluctuating pressure is defined as:

$$p'(t) = p(t) - \overline{p} \tag{2}$$

Fluctuating pressure allows a better identification of pressure waves because these are not masked by the pressure rise occurring in the impeller passage.

Figure 8 depicts 4 snapshots of the same impeller passages for 109 g/s case, colored by fluctuating pressure (see Eq. 2). The flow field is depicted at 50% span surface. This surface of revolution is unwrapped by projecting it on a normalized-meridional vs. circumferential plane (Drela and Youngren, 2008), resulting in the so-called blade-to-blade view. Figure 8 covers a temporal evolution of one main blade passing period.

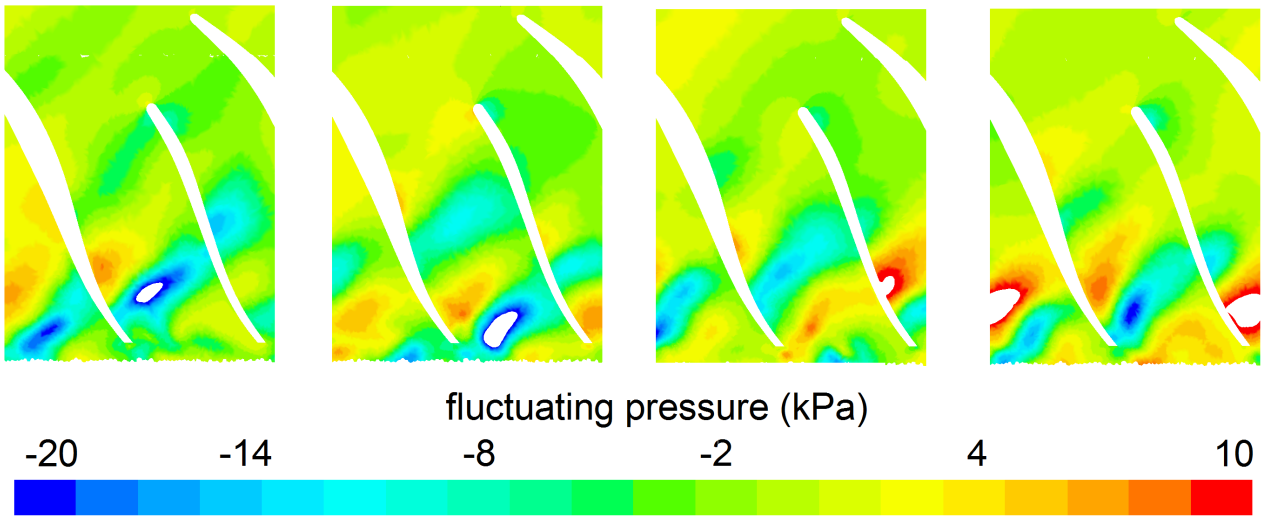

Figure 8: **Snapshots of temporal evolution (from left to right) of fluctuating pressure contours at 50% span blade-to-blade surface for 109 g/s case. The timespan is one main blade passing period.**

Pressure waves can be seen along the passages in Fig. 8, traveling in the streamwise direction, increasing their amplitude as they reach the exducer (with fluctuating pressure amplitudes of more than 30 kPa). Since the peaks and valleys of fluctuating pressure are at a similar position after a main blade passing period, this noise source should act as a narrow band centered at the main blade passing frequency (BPF). Figure 9 displays the PSD obtained by a point probe located at the trailing edge SS and linked to the relative reference frame. The aforementioned narrow band is detected at 16 kHz (BPF).

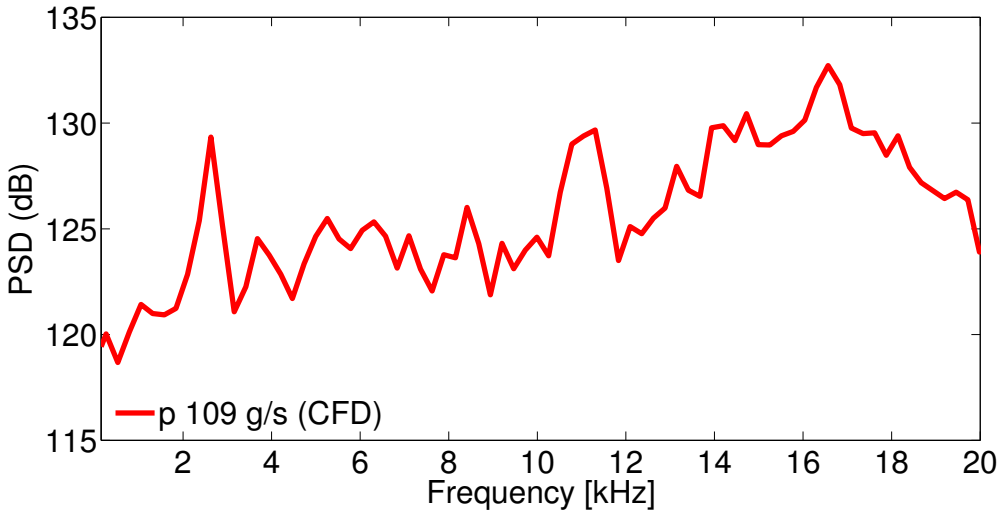

Figure 9: **PSD at the trailing edge suction side for 109 g/s operating point.**

Figure 10 shows a snapshot of the same instant considering different fluid variables so as to give an explanation for the phenomenon depicted in Fig. 8.

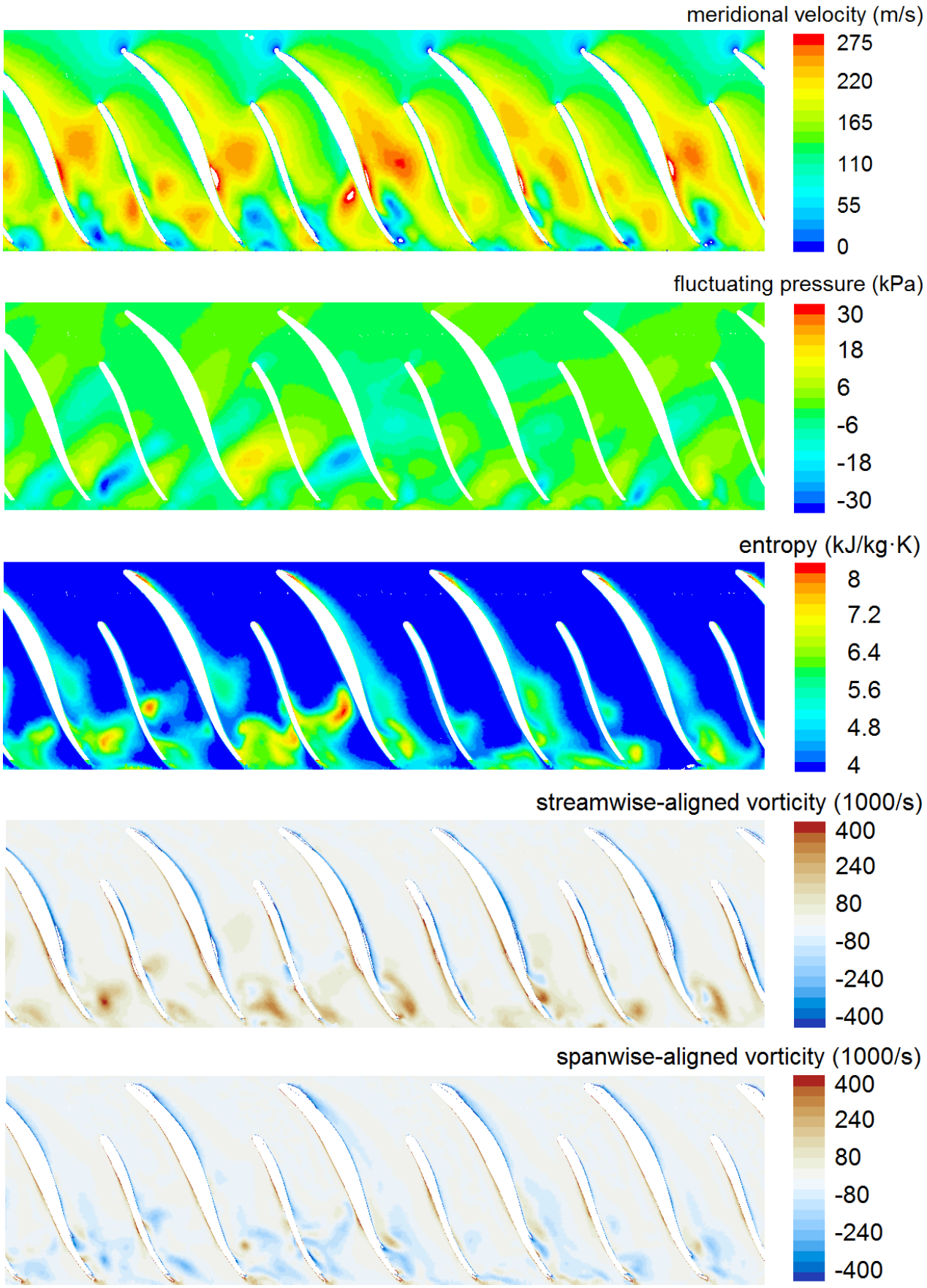

Figure 10: **Snapshot of 109 g/s case flow field variables at 50% span blade-to-blade surface.**

Meridional velocity contours reveal stall zones at blade suction side (see Fig. 10). The boundary layer is detached, and isolated streams of high velocity can be found at the pressure side. The separated boundary layer is unstable, and the blade passing seems to tune the boundary layer to detach and reattach at this particular frequency. This periodic behavior would therefore be the root cause of the aforementioned noise source.

Entropy contours at Fig. 10 shows that the effect of the suction side boundary layer is patent even in the leading edge. However, a sudden entropy rise is found at the same location at which the fluctuating pressure is more intense and stall zones exist, i.e., at the impeller exducer. At this location, positive streamwise-aligned vorticity (see Fig. 10) finds its maximums as well. In fact, entropy and streamwise-aligned vorticity snapshots are much alike. Spanwise-aligned vorticity is also greatest at the exducer, although negative and positive maximum values are both present to a similar extent, suggesting the formation of pairs of counter-rotating vortices.

A periodic oscillation of the separated boundary layer has been investigated by several researchers in axial turbomachinery (Wissink and Rodi, 2008), but, to the authors' knowledge, it has never been reported in centrifugal compressors. However, the results shown in this paper should be interpreted with care. Navarro (2014) showed that DES is working in LES mode at impeller passages core. The boundary layer functions in the URANS branch, which could lead to poor resolution of these periodic instabilities. Full LES simulations may be required for improving the accuracy of the simulations at BEP.

Besides, the mesh independence study was performed at an operating point close to surge, so the 9.5 million cells grid may not be fine enough to resolve properly this phenomenon at 109 g/s case, which would also explain the differences in pressure spectra represented in Fig. 5. In any case, BEP is the least noisy of the three operating conditions studied (see Figs. 5 to 7), so the loss of accuracy of the acoustic signature prediction at this point is not so relevant, being this the reason why the mesh independence study was conducted in near-surge conditions.

CONCLUSIONS

Turbocharger noise is becoming one of the most relevant sources of noise in automotive applications. In this paper, the mean flow and aeroacoustics of a centrifugal compressor at three different operating points from close to surge to best efficiency have been investigated. The model has been build from scanned surfaces and meshed with 9.5 million polyhedral cells. Detached-Eddy Simulation has been selected as turbulence modeling approach. Experiments have been carried out in an anechoic chamber in order to register the acoustic signature of the different working conditions. A methodology for a proper comparison between the measured and calculated spectra using the plane wave decomposition based on the Method of Characteristics.

Three different operating points have been analyzed at 160 krpm from near-surge conditions to best efficiency point. The analysis of the averaged flow shows how the recirculating zone near the shroud enlarges towards the compressor inlet as mass flow rate is reduced. For the studied point closest to surge, the recirculation reaches one diameter upstream the inducer. The positive incidence angle is responsible for the inception of the backflow.

Operating conditions become noisier as they get closer to surge. Simulations are quite accurate reproducing the compressor acoustic signature, although PSD is overpredicted for best efficiency point at plane wave range. An analysis of the transient flow field of best efficiency point at 160 krpm shows a periodic detachment and reattachment of the suction side boundary layer. This phenomenon seems tuned by the blade passing, resulting in a narrow band noise centered at the BPF for a probe linked to the reference frame.

REFERENCES

References

Andersen, J., Lindström, F., and Westin, F. (2008). Surge definitions for radial compressors in automotive turbochargers. *SAE International Journal of Engines*, 1(1):218–231.

Bousquet, Y., Carbonneau, X., Dufour, G., Binder, N., and Trebinjac, I. (2014). Analysis of the Unsteady Flow Field in a Centrifugal Compressor from Peak Efficiency to Near Stall with Full-Annulus Simulations. *International Journal of Rotating Machinery*, 2014:11.

Braun, M., Walsh, S., Horner, J., and Chuter, R. (2013). Noise source characteristics in the ISO 362 vehicle pass-by noise test: Literature review. *Applied Acoustics*, 74(11):1241–1265.

Broatch, A., Galindo, J., Navarro, R., and García-Tíscar, J. (2014). Methodology for experimental validation of a CFD model for predicting noise generation in centrifugal compressors. *International Journal of Heat and Fluid Flow*, 50:134–144.

Broatch, A., Galindo, J., Navarro, R., García-Tíscar, J., Daglish, A., and Sharma, R. K. (2015). Simulations and measurements of automotive turbocharger compressor whoosh noise. *Engineering Applications of Computational Fluid Mechanics*.

Cabral, B. and Leedom, L. C. (1993). Imaging vector fields using line integral convolution. In *Proceedings of the 20th annual conference on Computer graphics and interactive techniques*, pages 263–270. ACM.

Dehner, R., Figurella, N., Selamet, A., Keller, P., Becker, M., Tallio, K., Miazgowicz, K., and Wade, R. (2013). Instabilities at the low-flow range of a turbocharger compressor. *SAE International Journal of Engines*, 6(2):1356–1367.

Drela, M. and Youngren, H. (2008). *A User's Guide to MISES 2.63*. MIT Aerospace Computational Design Laboratory.

Evans, D. and Ward, A. (2005). Minimizing Turbocharger Whoosh Noise for Diesel Powertrains. *SAE Technical Paper*, 2005-01-2485.

Fontanesi, S., Paltrinieri, S., and Cantore, G. (2014). Cfd analysis of the acoustic behavior of a centrifugal compressor for high performance engine application. *Energy Procedia*, 45(0):759–768. ATI 2013 - 68th Conference of the Italian Thermal Machines Engineering Association.

Galindo, J., Serrano, J., Guardiola, C., and Cervelló, C. (2006). Surge limit definition in a specific test bench for the characterization of automotive turbochargers. *Experimental Thermal and Fluid Science*, 30(5):449–462.

Galindo, J., Tiseira, A., Navarro, R., and López, M. (2015). Influence of tip clearance on flow behavior and noise generation of centrifugal compressors in near-surge conditions. *International Journal of Heat and Fluid Flow*, 52:129–139.

Mendonça, F., Baris, O., and Capon, G. (2012). Simulation of Radial Compressor Aeroacoustics using CFD. In *Proceedings of ASME Turbo Expo 2012*, number GT2012-70028, pages 1823–1832. ASME.

Navarro, R. (2014). *A numerical approach for predicting flow-induced acoustics at near-stall conditions in an automotive turbocharger compressor*. PhD thesis, Universitat Politècnica de València.

Piñero, G., Vergara, L., Desantes, J., and Broatch, A. (2000). Estimation of velocity fluctuation in internal combustion engine exhaust systems through beamforming techniques. *Measurement Science & Technology*, 11(11):1585–1595.

Sevginer, C., Arslan, M., Sonmez, N., and Yilmaz, S. (2007). Investigation of turbocharger related whoosh and air blow noise in a diesel powertrain. In *Proceedings of the 36th International Congress and Exposition on Noise Control Engineering 2007*, pages 476–485.

Shur, M. L., Spalart, P. R., Strelets, M. K., and Travin, A. K. (2008). A hybrid RANS-LES approach with delayed-DES and wall-modelled LES capabilities. *International Journal of Heat and Fluid Flow*, 29(6):1638–1649.

STAR-CCM+ (2014). CD-adapco, release version 9.02.005 edition.

Stoffels, H. and Schroeer, M. (2003). NVH Aspects of a Downsized Turbocharged Gasoline Powertrain with Direct Injection. *SAE Technical Paper*, 2003-01-1664.

Teng, C. and Homco, S. (2009). Investigation of Compressor Whoosh Noise in Automotive Turbochargers. *SAE Int. J. of Passeng. Cars-Mech. Syst.*, 2(1):1345–1351.

Torregrosa, A. J., Fajardo, P., Gil, A., and Navarro, R. (2012). Development of a non-reflecting boundary condition for application in 3D computational fluid dynamic codes. *Engineering Applications of Computational Fluid Mechanics*, 6(3):447–460.

Welch, P. (1967). The use of fast fourier transform for the estimation of power spectra: a method based on time averaging over short, modified periodograms. *Audio and Electroacoustics, IEEE Transactions on*, 15(2):70–73.

Wissink, J. G. and Rodi, W. (2008). The influence of periodically incoming wakes on the separating flow in a compressor cascade. In *High Performance Computing in Science and Engineering'08: Transactions of the High Performance Computing Center, Stuttgart (HLRS)*, pages 205–215. Springer.